Research Article | Vol. 8, No. 3 | 1 Mar 2018 | OPTICAL MATERIALS EXPRESS 629
Optical Materials EXPRESS

High index contrast passive potassium double tungstate waveguides

MUSTAFA AKIN SEFUNC, FRANS B. SEGERINK, AND SONIA M. GARCÍA-BLANCO*

Optical Sciences Group, MESA + Institute for Nanotechnology, University of Twente, P.O. Box 217, 7500 AE, Enschede, The Netherlands
**s.m.garciablanco@utwente.nl*

Abstract: High-refractive-index-contrast potassium double tungstate waveguides have been experimentally demonstrated. A bulk $KY(WO_4)_2$ layer was successfully bonded onto a lower refractive index carrier using a UV curable optical adhesive and polished down to the thickness of 2.4 μm. A set of rib waveguides with ~2 μm width and 0.85 μm slab thickness were fabricated on the thin transferred $KY(WO_4)_2$ layer by focused-ion-beam milling. The upper-limit of the propagation losses of the fabricated waveguides is estimated to be 1.5 dB/cm at the wavelength of 1.55 μm using the Fabry-Perot method.

OCIS codes: (130.0130) Integrated optics; (220.0220) Optical design and fabrication; (230.7370) Waveguides; (120.2230) Fabry-Perot; (220.5450) Polishing.

References and links

1. S. A. Vázquez-Córdova, M. Dijkstra, E. H. Bernhardi, F. Ay, K. Wörhoff, J. L. Herek, S. M. García-Blanco, and M. Pollnau, "Erbium-doped spiral amplifiers with 20 dB of net gain on silicon," Opt. Express **22**(21), 25993–26004 (2014).
2. I. Vasilief, S. Guy, B. Jacquier, B. Boulard, Y. P. Gao, C. Duverger, H. Haquin, V. Nazabal, J.-L. Adam, M. Couchaud, L. Fulbert, C. Cassagnettes, F. Rooms, and D. Barbier, "Propagation losses and gain measurements in erbium-doped fluoride glass channel waveguides by use of a double-pass technique," Appl. Opt. **44**(22), 4678–4683 (2005).
3. A. A. Reddy, S. S. Babu, K. Pradeesh, C. J. Otton, and G. Vijaya Prakash, "Optical properties of highly Er^{3+}-doped sodium–aluminium–phosphate glasses for broadband 1.5 μm emission," J. Alloys Compd. **509**(9), 4047–4052 (2011).
4. E. Snoeks, G. N. Van Den Hoven, A. Polman, B. Hendriksen, M. B. J. Diemeer, and F. Priolo, "Cooperative upconversion in erbium-implanted soda-lime silicate glass optical waveguides," J. Opt. Soc. Am. **12**(8), 1468 (1995).
5. K. Petermann, D. Fagundes-Peters, J. Johannsen, M. Mond, V. Peters, J. J. Romero, S. Kutovoi, J. Speiser, and A. Giesen, "Highly Yb-doped oxides for thin disc lasers," J. Cryst. Growth **275**(1–2), 135–140 (2005).
6. N. V. Kuleshov, A. A. Lagatsky, A. V. Podlipensky, V. P. Mikhailov, A. A. Kornienko, E. B. Dunina, S. Hartung, and G. Huber, "Fluorescence dynamics, excited-state absorption, and stimulated emission of Er^{3+} in $KY(WO_4)_2$," J. Opt. Soc. Am. B **15**(3), 1205–1212 (1998).
7. D. Geskus, S. Aravazhi, S. M. García-Blanco, and M. Pollnau, "Giant optical gain in a rare-earth-ion-doped microstructure," Adv. Mater. **24**(10), OP19–OP22 (2012).
8. K. van Dalfsen, S. Aravazhi, C. Grivas, S. M. García-Blanco, and M. Pollnau, "Thulium channel waveguide laser with 1.6 W of output power and ~80% slope efficiency," Opt. Lett. **39**(15), 4380–4383 (2014).
9. S. Aravazhi, D. Geskus, K. van Dalfsen, S. A. Vázquez-Córdova, C. Grivas, U. Griebner, S. M. García-Blanco, and M. Pollnau, "Engineering lattice matching, doping level, and optical properties of $KY(WO_4)_2$:Gd,Lu,Yb layers for a cladding-side-pumped channel waveguide laser," Appl. Phys. B **111**(3), 433–446 (2013).
10. G. Roelkens, L. Liu, D. Liang, R. Jones, A. Fang, B. Koch, and J. Bowers, "III-V/silicon photonics for on-chip and inter-chip optical interconnects," Laser Photonics Rev. **4**(6), 751–779 (2010).
11. L. Chang, M. H. P. Pfeiffer, N. Volet, M. Zervas, J. D. Peters, C. L. Manganelli, E. J. Stanton, Y. Li, T. J. Kippenberg, and J. E. Bowers, "Heterogeneous integration of lithium niobate and silicon nitride waveguides for wafer-scale photonic integrated circuits on silicon," Opt. Lett. **42**(4), 803–806 (2017).
12. S. Ghosh, S. Keyvaninia, W. Van Roy, T. Mizumoto, G. Roelkens, and R. Baets, "Adhesively bonded Ce:YIG/SOI integrated optical circulator," Opt. Lett. **38**(6), 965–967 (2013).
13. G. Roelkens, J. Brouckaert, D. Van Thourhout, R. Baets, R. Nötzel, and M. Smit, "Adhesive bonding of InP/InGaAsP dies to processed silicon-on-insulator wafers using DVS-bis-benzocyclobutene," J. Electrochem. Soc. **153**(12), G1015–G1019 (2006).

#315015 https://doi.org/10.1364/OME.8.000629
Journal © 2018 Received 5 Dec 2017; revised 29 Jan 2018; accepted 4 Feb 2018; published 14 Feb 2018

Optical Materials EXPRESS

14. S. Matsuo, K. Tateno, T. Nakahara, H. Tsuda, and T. Kurokawa, "Use of polyimide bonding for hybrid integration of a vertical cavity surface emitting laser on a silicon substrate," Electron. Lett. **33**(13), 1148–1149 (1997).
15. F. J. Blanco, M. Agirregabiria, J. Garcia, J. Berganzo, M. Tijero, M. T. Arroyo, J. M. Ruano, I. Aramburu, and K. Mayora, "Novel three-dimensional embedded SU-8 microchannels fabricated using a low temperature full wafer adhesive bonding," J. Micromech. Microeng. **14**(7), 1047–1056 (2004).
16. M. A. Sefunc, F. Segerink, and S. Garcia-Blanco, "High index contrast potassium double tungstate waveguides towards efficient rare-earth ion amplification on-chip," Proc. SPIE **9365**, 93650P (2015).
17. P. A. Loiko, K. V. Yumashev, N. V. Kuleshov, G. E. Rachkovskaya, and A. A. Pavlyuk, "Detailed characterization of thermal expansion tensor in monoclinic $KRe(WO_4)_2$ (where Re = Gd, Y, Lu, Yb)," Opt. Mater. **34**(1), 23–26 (2011).
18. U. Gosele and Q.-Y. Tong, "Semiconductor Wafer Bonding," Annu. Rev. Mater. Sci. **28**(1), 215–241 (1998).
19. T. R. Chung, L. Yang, N. Hosoda, and T. Suga, "Room temperature GaAs-Si and InP-Si wafer direct bonding by the surface activated bonding method," Nucl. Instruments Methods Phys. Res. Sect. B Beam Interact with Mater. Atoms **121**, 203–206 (1997).
20. C.-T. Ko, K.-N. Chen, G. Cha, R. Gafiteanu, and U. Gosele, "Low temperature bonding technology for 3D integration," Microelectron. Reliab. **3**(1), 29–35 (1994).
21. W. Bolaños, J. J. Carvajal, X. Mateos, G. S. Murugan, A. Z. Subramanian, J. S. Wilkinson, E. Cantelar, D. Jaque, G. Lifante, M. Aguiló, and F. Díaz, "Mirrorless buried waveguide laser in monoclinic double tungstates fabricated by a novel combination of ion milling and liquid phase epitaxy," Opt. Express **18**(26), 26937–26945 (2010).
22. F. Ay, I. Iñurrategui, D. Geskus, S. Aravazhi, and M. Pollnau, "Integrated lasers in crystalline double tungstates with focused-ion-beam nanostructured photonic cavities," Laser Phys. Lett. **8**(6), 423–430 (2011).
23. Y. Okamura, S. Yoshinaka, and S. Yamamoto, "Measuring mode propagation losses of integrated optical waveguides: a simple method," Appl. Opt. **22**(23), 3892 (1983).
24. M. D. Himel and U. J. Gibson, "Measurement of planar waveguide losses using a coherent fiber bundle," Appl. Opt. **25**(23), 4413–4416 (1986).
25. H. P. Weber, F. A. Dunn, and W. N. Leibolt, "Loss measurements in thin-film optical waveguides," Appl. Opt. **12**(4), 755–757 (1973).
26. G. Tittelbach, B. Richter, and W. Karthe, "Comparison of three transmission methods for integrated optical waveguide propagation loss measurement," Pure Appl. Opt. J. Eur. Opt. Soc. Part A **2**(6), 683–700 (1993).
27. A. Rickman, G. T. Reed, B. L. Weiss, and F. Namavar, "Low-loss planar optical waveguides fabricated in SIMOX material," IEEE Photonics Technol. Lett. **4**(6), 633–635 (1992).
28. I. P. Kaminow and L. W. Stulz, "Loss in cleaved Ti-diffused $LiNbO_3$ waveguides," Appl. Phys. Lett. **33**(1), 62–64 (1978).
29. S. Taebi, M. Khorasaninejad, and S. S. Saini, "Modified Fabry-Perot interferometric method for waveguide loss measurement," Appl. Opt. **47**(35), 6625–6630 (2008).
30. D. F. Clark and M. S. Iqbal, "Simple extension to the Fabry-Perot technique for accurate measurement of losses in semiconductor waveguides," Opt. Lett. **15**(22), 1291–1293 (1990).
31. D. Geskus, S. Aravazhi, C. Grivas, K. Wörhoff, and M. Pollnau, "Microstructured $KY(WO_4)_2$:Gd^{3+}, Lu^{3+}, Yb^{3+} channel waveguide laser," Opt. Express **18**(9), 8853–8858 (2010).
32. C. N. Borca, V. Apostolopoulos, F. Gardillou, H. G. Limberger, M. Pollnau, and R. P. Salathé, "Buried channel waveguides in Yb-doped $KY(WO_4)_2$ crystals fabricated by femtosecond laser irradiation," Appl. Surf. Sci. **253**(19), 8300–8303 (2007).
33. A. Choudhary, W. Bolaños, P. Kannan, J. J. Carvajal, M. Aguiló, F. Diaz, and D. P. Shepherd, "Low-threshold, mirrorless emission at 981 nm in an Yb,Gd,Lu:KYW inverted rib waveguide laser," Proc. SPIE **8599**, 859905 (2013).

1. Introduction

The family of monoclinic potassium double tungstates, $KY(WO_4)_2$, $KGd(WO_4)_2$ and $KLu(WO_4)_2$, are excellent host materials for lanthanide ions (Yb^{3+}, Er^{3+}, Gd^{3+}, Lu^{3+}, etc.) thanks to their optical properties such as high refractive index (n~2) in comparison with other host materials—Al_2O_3 [1], fluoride [2], phosphate [3] and soda-lime silicate [4] glasses—high thermal conductivity (~3.3 $Wm^{-1}K^{-1}$) [5], and high emission and absorption cross-sections for the lanthanide ions doped into these materials [6]. The crystalline structure of the potassium double tungstates offers sufficient inter-ionic distance between the active ions in the crystal lattice (~0.5 nm) so that clustering of doped ions can be prevented. As a result, high modal gain (circa 1000 dB/cm) in an Yb^{3+} doped waveguide amplifier [7] as well as efficient (~80%) high power (~1.6 W) waveguide lasers at ~2 μm [8] have recently being reported in a low-contrast waveguide configuration. These devices have been fabricated on rare-earth ion

Optical Materials EXPRESS

doped layers grown onto undoped $KY(WO_4)_2$ substrates by liquid phase epitaxy [9]. The refractive index contrast between the doped and undoped layers is typically smaller than 0.02.

Low contrast waveguides have several disadvantages, such as large mode field diameter (i.e., ranging from 6 μm [7] to 25 μm [8]), large bend radii and long devices (i.e., typically a few millimeters), which make them not suitable for integration with other optical functions onto different passive photonic technology platforms such as silicon-on-insulator or Si_3N_4 on SiO_2. High-contrast waveguides (i.e., refractive index difference between core and cladding of >0.5), on the other hand, exhibit a tight field confinement in the core, which enhances light-matter interaction, reducing the pump power requirements to achieve inversion of the material and enabling the exploitation of non-linear effects that would require too high power in a low-contrast waveguide configuration. However, the crystalline nature of the double tungstate host materials is disadvantageous for the integration with low refractive index dielectrics, such as SiO_2, required for the realization of high-contrast waveguides. Direct growth of crystalline $KY(WO_4)_2$ material onto amorphous substrates is prevented by the requirement of lattice matching to achieve optical quality crystalline layers [9]. Heterogeneous integration has been developed in recent years for the integration of dissimilar materials including III-V semiconductors on silicon [10], $LiNbO_3$ on silicon nitride [11], and magnetorresistive materials on silicon [12]. Either direct bonding technique [10] or adhesive bonding, typically with bonding material such as bencocyclobutene (BCB) [13], polyimide [14] or SU8 [15] are the techniques typically employed.

In this work, high-refractive-index-contrast passive $KY(WO_4)_2$ waveguides are demonstrated for the first time. The waveguides are fabricated by heterogeneous transfer of a thin $KY(WO_4)_2$ layer followed by focused-ion-beam (FIB) milling of the rib waveguides [16]. The propagation losses of the fabricated waveguides are estimated from the measured reflected Fabry-Perot fringes. In the following sections, the steps for the fabrication of high-contrast $KY(WO_4)_2$ waveguides will be explained in detail. Propagation losses <1.5 dB/cm were achieved for high contrast uncladded waveguides.

2. Fabrication of high-contrast rib $KY(WO_4)_2$ waveguides

A new micro-fabrication process flow has been developed to realize high-contrast passive $KY(WO_4)_2$ waveguides. $KY(WO_4)_2$ substrates 1 mm thick and with 1x1 cm^2 surface area are purchased from Altechna (LT). The monoclinic $KY(WO_4)_2$ crystal has three optical axes [9] as well as different coefficients of thermal expansion along the different optical axes [17].

The fabrication process flow can be divided into three main processing steps: (1) bonding the $KY(WO_4)_2$ onto a SiO_2 carrier chip; (2) thinning of the bonded material to the required thickness, which defines the waveguide height; and (3) ion beam milling of rib waveguides.

2.1 Bonding

When the thermal expansion coefficients of the substrate and the bonded sample are significantly different from each other, the stress on the bonding interface causes cracks and/or delamination either on the bonded layer or on the substrate layer. Typical adhesive bonding methods require relatively high temperatures (> 100°C) to achieve a strong adhesion between sample and substrate. In direct bonding, spontaneous adhesion via van der Waals forces between two ultra-smooth (<0.5 nm rms) and ultra-flat materials [18] permits permanent bonding between two dissimilar materials. Although the bonding process in some cases can take place at room temperature [19], usually a post-bond annealing step (200°C – 400°C) is still required to form strong chemical bonds and ensure high bonding strength [20]. In this work, the UV curable adhesive material NOA81 (Norland Products Inc., USA) is used to eliminate the requirement of elevated bonding temperature while providing high bonding strength.

The bonding process starts by cleaning a 2 cm by 2 cm, 0.5 mm thick fused silica carrier substrate and a 1 mm thick $KY(WO_4)_2$ sample with lateral dimensions of 1 cm by 1 cm in an

Optical Materials EXPRESS

ultrasonic bath filled with DI water for 15 minutes in order to remove particles on the surfaces. The sample and the carrier are then chemically cleaned in 99% HNO_3 for 10 minutes. A NOA 81 adhesive layer is then spin-coated on the $KY(WO_4)_2$ sample using a two-step process: 500 rpm for 5 seconds followed by 4000 rpm for 20 seconds. The spinning process gives a ~6.5 µm thick adhesive layer. The adhesive layer is then pre-cured under a hand-held UV light source (peak wavelength ~365 nm) with an intensity of 50 µJ/cm^2 for 5 seconds. This process step increases the viscosity of the adhesive liquid, which reduces the spreading of excess liquid from the corners of the sample during the bonding step. The bonding between fused silica carrier and undoped $KY(WO_4)_2$ is realized in a Finetech Lambda flip-chip bonder (Finetech GmbH, DE) with a nominal placement accuracy of 0.5 µm applying 10 N of bonding force. A ~6 µm thick adhesive layer is obtained at the bonding interface. The adhesive material residues on the carrier and on the corners of the $KY(WO_4)_2$ are removed in an oxygen plasma (50% 200 sccm O_2 flow with 500 W plasma power for 10 minutes under 1.2 mbar pressure). The bonded sample is then exposed to UV light for a total fluence of 2 J/cm^2 to fully cure the adhesive layer between the sample and substrate. Finally, the sample surface is cleaned with ethanol for 5 minutes to dissolve any adhesive material residues decomposed in the oxygen plasma step.

2.2 Thinning

A thinning step is required to reduce the thickness of the bonded 1 mm thick $KY(WO_4)_2$ material to the required waveguide thickness. The thinning process consists of two steps. A first coarse lapping step reduces the sample thickness rapidly to ~15 µm. It is followed by a polishing step to slowly obtain an optical-quality layer of the target thickness. The thinning was performed using a Logitech PM5 precision lapping and polishing system (Logitech, UK). The bonded sample was fixed on a 5.75 mm thick ultra-parallel glass plate with Alcowax (Nikka Seiko, JP). The corners of the $KY(WO_4)_2$ sample were also covered with wax to avoid any undesirable cracks appearing during the thinning process. In the lapping step, a non-drying colloidal silica suspension with 9 µm diameter particles was utilized. During the polishing process, a slurry with 40 nm size particles was utilized (OP-U polishing suspension, Struers, DE). The layer thickness is aimed at supporting a single transverse electric (TE) mode at the operation wavelength (λ = 1.55 µm), for which a $KY(WO_4)_2$ layer of <2.5 µm is required according to finite-difference (FD) mode simulations. Figure 1(a) shows an image of a thin $KY(WO_4)_2$ layer transferred onto a SiO_2 substrate. The thicknesses of the adhesive and $KY(WO_4)_2$ layers are ~6 µm and ~2.4 µm respectively. The RMS surface roughness of the polished surface is as low as 0.17 nm according to atomic force microscope measurements [Fig. 1(b)]. The sample was diced from the two sides to create direct access to the $KY(WO_4)_2$ layer.

Optical Materials EXPRESS

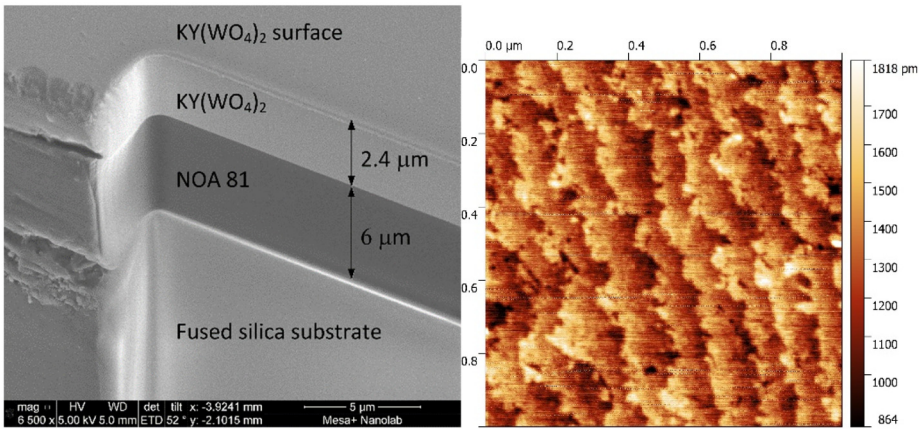

(a) (b)

Fig. 1. (a) End-facet of a thin (2.4 µm) $KY(WO_4)_2$ layer bonded onto a fused silica substrate by NOA81 adhesive. The end-facet has been polished using focused ion beam; (b) Atomic force microscope AFM) scan of the surface of the transferred $KY(WO_4)_2$ layer (AFM Fast Scan, Bruker, DE). A 0.9x0.9 μm^2 area was scanned with an 8 nm radius tip. The surface root-mean-square roughness is as low as 0.17 nm.

2.3 Waveguide patterning

Numerous reports describe the patterning of $KY(WO_4)_2$ by ion beam etching (IBE) technique [7-8, 21]. However, the lateral resolution is limited by the required thickness of the resist used as etch mask. In focused-ion-beam milling (FIB), accelerated gallium ions are used to sputter the material and it can be utilized to pattern optical structures with nanometer resolution [22]. FIB milling is a serial technique and therefore not suited for mass-production applications. In this work, FIB was used to develop the first proof-of-concept high-contrast waveguides in $KY(WO_4)_2$.

Optical Materials EXPRESS

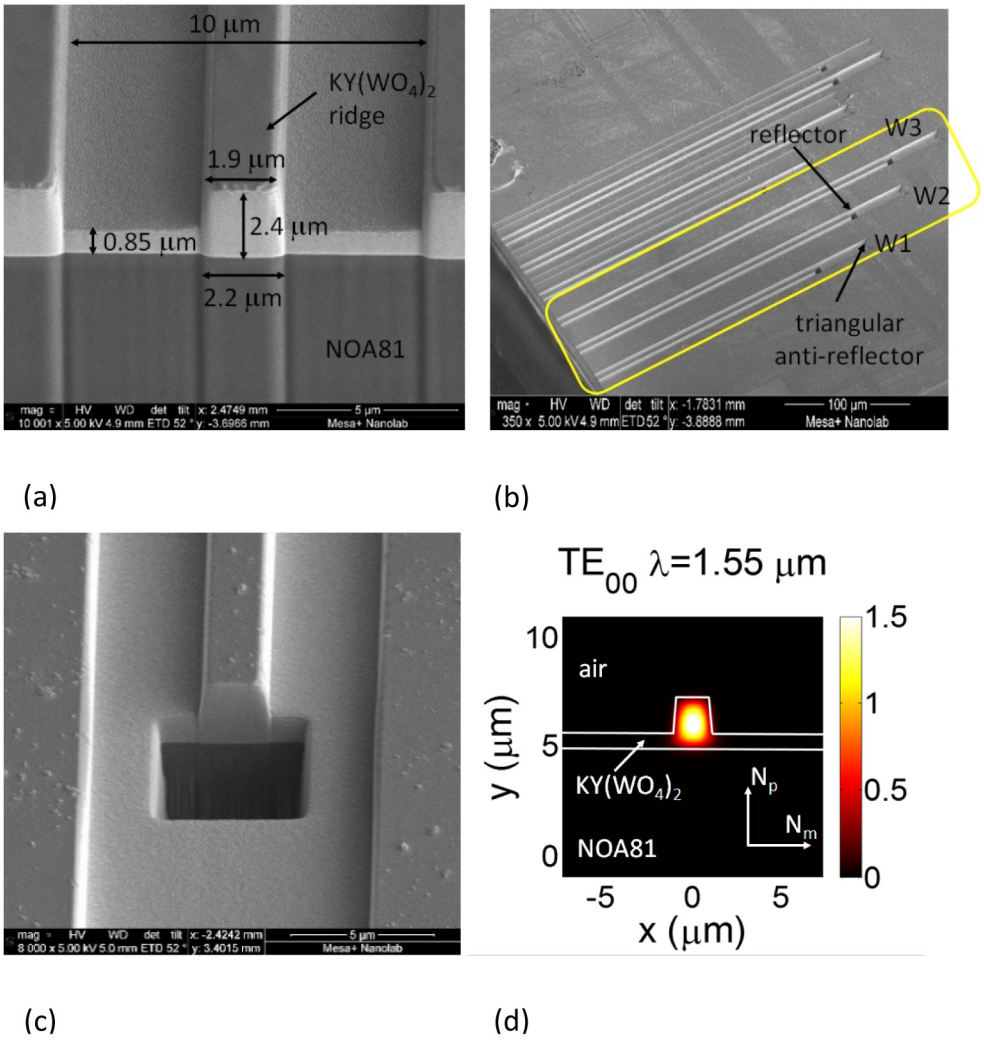

Fig. 2. (a) Scanning electron microscope (SEM) image of the cross-section of a FIB milled rib passive $KY(WO_4)_2$ channel waveguide. The corresponding dimensions are given on the image; (b) Tilted SEM image of the waveguides on the layer. The waveguides covered with a yellow solid line with labels "W1", "W2" and "W3" were characterized in this study. The length of the "W1", "W2" and "W3" waveguides are 200 μm, 250 μm and 300 μm, respectively. At the end of each waveguide, a reflector is etched to ensure the same reflectivity from both waveguide end-facets. Triangular anti-reflectors are etched away at the end of the waveguides to minimize the possible reflection that goes back to the waveguide end-facets; (c) SEM image of the deep reflectors at the output end-facets; (d) Simulated 2-D transverse-electric (TE) mode profile at the cross-section of the rib waveguide given at λ = 1.55 μm. The optical axes of the $KY(WO_4)_2$ crystal are shown. The calculated effective refractive index is 1.9492 at the wavelength of 1.55 μm.

Two-dimensional (2-D) FD mode calculations were carried out using OptoDesigner (Phoenix Software BV, NL) to find the cross-sectional dimensions of the waveguides that support single mode propagation at the operation wavelength. Rib waveguides with a width of ~2 μm, thickness 2.4 μm and slab height of 0.85 μm [Fig. 2(a)] were fabricated on a transferred $KY(WO_4)_2$ layer. The waveguides were aligned along the N_g axis. Sets of waveguides with lengths of 300 μm, 250 μm and 200 μm were produced [Fig. 2(b)]. The milling beam current was set to 2.7 nA to obtain high quality, low roughness waveguide

Optical Materials EXPRESS

sidewalls within a reasonable process time (2 hours 20 minutes for a set of three waveguides). In order to minimize processing time, the waveguides were placed inside a 10 μm wide trench as shown in Fig. 2(a). According to the FD mode calculations, the trench width is sufficient to prevent any cross-talk between adjacent waveguides. The patterning was followed by FIB polishing of the input and output facets to ensure high and equal reflectivity from input [Fig. 2(a)] and output [Fig. 2(c)] waveguide end-facets. Figure 2(d) shows the simulated mode profile supported at the cross-section of the rib waveguides. Table 1 shows the refractive indices of the different materials utilized for the simulations.

Table 1. Refractive indices of the materials utilized in the simulations, indicating the Sellmeier equation utilized to fit the refractive index and its coefficients. Lambda in micrometers.

Material	Sellmeier equation	A	B	C
NOA*	$n = A + B/\lambda^2 + C/\lambda^4$	1.5375	8.290×10^{-3}	-2.11046×10^{-4}
KYW (N_m axis) [9]	$n = \mathrm{sqrt}(A + B\lambda^2/(\lambda^2-C))$	1	2.9568303	0.02534002

*Data from the datasheet of the NOA61

3. Characterization of waveguides using the Fabry-Perot method

Various methods are typically used to estimate the propagation losses of optical waveguides, including the measurement of the waveguide scattered light streak [23,24], the prism-coupling method [25], insertion loss measurement method [26, 27], and the cut-back method [28]. The aforementioned methods are, however, not suitable for the study of the losses of the short waveguides fabricated in this work. The method based on the measurement of the waveguide scattered light streak depends strongly on the quality of the device surface and the confinement of the waveguide architecture. In the particular case of this work, the short length of the waveguides makes the scattering from the incoupling spot overrun the limited scattering along the waveguide streak due to the high confinement of the waveguide mode. The other methods rely on transmission measurements, which are not possible in the waveguides of this work [Fig. 2 (b)]. Propagation losses can also be estimated based on the Fabry-Perot fringes induced in the waveguide cavity formed between the input and output end-facets [29-30].

The power reflected from the Fabry-Perot cavity by the end-facets of the waveguides is given by Eq. (1) [30]

$$P_R = \eta P_0 \frac{r^2 - 2r^2 e^{-2\alpha L}\cos\delta + r^2 e^{-4\alpha L}}{1 - 2r^2 e^{-2\alpha L}\cos\delta + r^4 e^{-4\alpha L}} + offset \qquad (1)$$

where δ defines the phase change accumulated in a round trip along the length of the waveguide, L, given by the relation $k_0 n_{eff} 2L$, k_0 is the free-space wavenumber ($2\pi/\lambda$), n_{eff} effective refractive index, which is calculated to be 1.9492 at 1.55 μm wavelength based on the refractive indices as a function of wavelength of the different materials (Table 1) and the measured dimensions of the waveguides [Fig. 2(a)] using the 2D FD mode solver, α is the propagation loss in cm^{-1}, P_0 is the incident beam power on the waveguide end-facet, η is the coupling coefficient, calculated as the mode overlap between the modes of the fiber and waveguide,and r is the wavelength dependent reflection coefficient of the end-facet, which has been approximated as the Fresnel reflection between a material with refractive index n_{eff} and air. The term *offset* defines the non-coupled power reflected from the input end-facet, which contributes as a DC offset to the measured signal (i.e., it therefore does not affect the quality of the fit of the waveguide losses). As mentioned above, FIB milling with Ga^+ ions was utilized to pattern the high-contrast $KY(WO_4)_2$ waveguides as well as to polish the input and output facets. A square deep trench larger than the size of the mode propagating in the waveguide was etched at the output end-facet to ensure the same reflectivity, r, in both end-

Optical Materials EXPRESS

facets [Fig. 2 (c)]. Identical waveguides were fabricated with different lengths—200 μm, 250 μm and 300 μm—in order to increase the confidence of the fit to the measured data.

The characterization setup consists of a coherent tunable light source with an InGaAs photodetector module (Agilent 8164B Lightwave measurement system with 81600B-201 laser module), and an optical circulator (OC). The OC is utilized to separate the input signal from the reflected signal coming from the $KY(WO_4)_2$ waveguides. The schematic of the characterization setup is depicted in Fig. 3. A tunable laser in the wavelength range of interest is connected to the first port of the OC by a single-mode (SM) polarization-maintaining (PM) fiber. The light coming from port 1 is guided to port 2 and then coupled to the waveguide using a bare PM fiber. The distance between the bare fiber and the end-facet of the waveguide was minimized (typically below 1 μm) to minimize the effect of the cavity formed between the fiber and end-facet, which will introduce a slow varying envelop to the measured data. The reflected light coming from the waveguide is circulated to port 3, where the power detector is connected to. Prior to measuring the response of the waveguide, a reference measurement of the characterization setup without the sample is taken to detect and store the reflections originating from the various cavities formed within the system, such as the fiber connections in the light source and the fiber-to-fiber interfaces across the OC. This reference measurement is subtracted from the measured Fabry-Perot reflection of the waveguide.

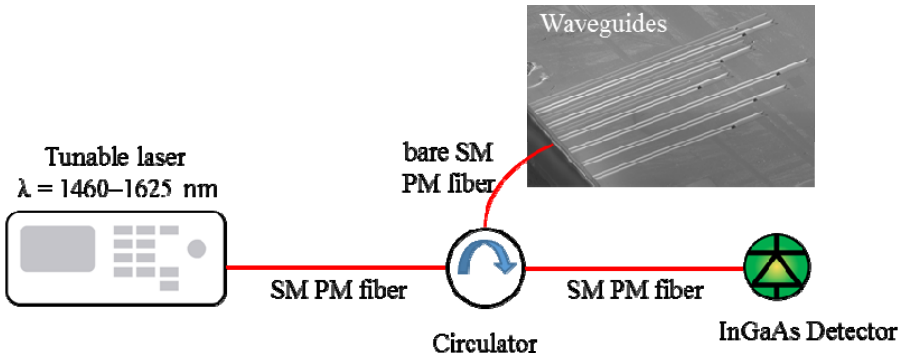

Fig. 3. Schematic of the optical setup built for the characterization of the propagation loss of $KY(WO_4)_2$ waveguides based on Fabry-Perot method around λ = 1.55 μm.

Figure 4 shows the measured reflections from the fabricated waveguides with 200 μm length (W1). The separation between the adjacent reflection peaks fits well to the different cavity lengths as expected from the free spectral range formula given as: $\Delta\lambda_{FSR} = \lambda^2/(n_g \ell)$, where n_g is the group refractive index of the cavity and ℓ is the roundtrip cavity length; $\ell = 2L$. The n_g obtained from these measurements, 2.06, 2.04 and 2.06 for waveguides W1, W2 and W3 respectively at a wavelength of 1.55 μm, agree well with the calculated value, 2.053 at 1.55 μm, for the measured waveguide cross-section. The high-frequency oscillations on the measured signals are mainly attributable to the cavity formed inside the bare fiber attached to port 2 of the OC. These oscillations were not filtered to avoid any distortions that would affect the result of the fitting. The data was fitted to the theoretical expression for the reflected power [Eq. (1)]. The incident power at the tip of the 9.9 μm-diameter SM fiber (P_0) is measured as 0.635 mW using an IR photodetector (Newport 818-IR photodetector). The coupling coefficient between the waveguide fundamental mode and the fiber is calculated as 0.127 using 2D-FD mode solver. The variables used in the fitting were the length, offset and the propagation losses. The results of the fit are shown in Table 2. An R^2 value of 0.94 was obtained for the fit. The offset values obtained agree well with expectations. A propagation loss <1.5 dB/cm for the measured wavelength range was obtained.

Optical Materials EXPRESS

The propagation losses achieved in this first demonstration of high-contrast waveguides in $KY(WO_4)_2$ are comparable to the reported propagation losses for low-contrast $KY(WO_4)_2$ channel waveguides in the literature. Geskus *et al.* fabricated channel waveguides with 0.34 dB/cm propagation loss at 1 μm on Gd^{3+} and Lu^{3+} co-doped $KY(WO_4)_2$:Yb^{3+} layer using Ar^+ ion beam milling [31]. Borca *et al.* reported on fabricating $KY(WO_4)_2$:Yb^{3+} waveguides using an ultrashort pulse laser writing, which leads to propagation losses in the range of 2.7 dB/cm at the same wavelength [33]. Several strategies can be implemented to further reduce the propagation losses. Firstly, it is important to note that the high-contrast waveguides in this work are air cladded, which makes the light propagation in the core more sensitive to particles and roughness of the sidewalls. A low refractive index cladding will be applied when the developed waveguides are used in a real device application, which is expected to reduce scattering losses. Furthermore, FIB milling relies on bombarding the surface to be sputtered with a finely focused beam of Ga^+ ions. The Ga^+ implantation at the waveguide sidewalls is inevitable in the patterning process, and it can also contribute to the measured propagation losses. Further work is underway to understand the effect of the Ga^+ implantation on propagation losses and ways to reduce its effect. Although FIB is not the most suitable method for the fabrication of long waveguides, the low losses achieved in this first demonstration show that this technique could be utilized for the realization of waveguide regions where dimensions below what can be achieved with standard UV lithography are required, such as in tapers or waveguide gratings. Work is currently under way to improve the thinning process to achieve thinner layers (<1 μm) in a reproducible manner. The ultimate objective is the realization of high-contrast waveguides with dimensions below 1 μm x1 μm.

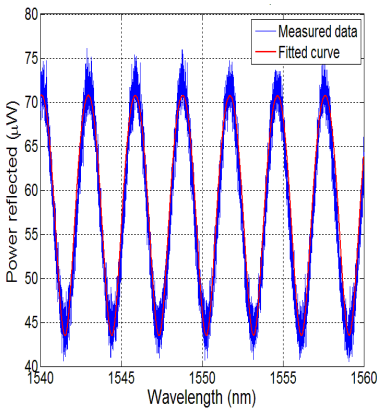

Fig. 4. Example of measured and fitted reflected signals from the FIB-patterned high-contrast waveguide. W2 (200 μm length).

Table 2. Parameters used for the fits to the measured data. R^2 of the fit, R^2 = 0.94.

Fitting parameters	Fitting values		
Length (*L*)	200.05 μm	250.16 μm	300.23 μm
Offset	44 μW	35 μW	22 μW
Propagation loss (*α*)	<1.5 dB/cm	<1.5 dB/cm	<1.5 dB/cm

4. Conclusion

In this work, the first high-refractive-index-contrast (Δn ≈0.45) $KY(WO_4)_2$ waveguides have been experimentally demonstrated. The waveguides were realized by a combination of an heterogeneous thin $KY(WO_4)_2$ layer transfer (via adhesive bonding followed by lapping and polishing) and focused-ion-beam milling. The propagation losses of the fabricated waveguides were estimated to be <1.5 dB/cm at a wavelength of 1.55 μm by analyzing the Fabry-Perot reflections of the cavity formed between the waveguide FIB polished end-facets.

Optical Materials EXPRESS

Funding

"Stichting voor de Technisch Wetenschappen" (STW) (STW-12832: "High-bit-rate on-chip nanoamplifiers in Er^{3+} doped double tungstates") and ERC Consolidator (grant project RENOS "Rare-earth doped novel on-chip sources"- 648978).